Geophysical Research Letters

RESEARCH LETTER
10.1029/2020GL087398

The Deformational Journey of the Nazca Slab From Seismic Anisotropy

Shubham Agrawal[1], Caroline M. Eakin[1], Daniel E. Portner[2,3], Emily E. Rodriguez[2], and Susan L. Beck[2]

[1]Research School of Earth Sciences, The Australian National University, Canberra, ACT, Australia, [2]Department of Geosciences, University of Arizona, Tucson, AZ, USA, [3]Department of Terrestrial Magnetism, Carnegie Institution of Washington, Washington, DC, USA

Key Points:
- We find a notable presence of anisotropy within the Nazca slab in both the upper and lower mantle
- Upper mantle slab anisotropy is strongest where the slab geometry is most contorted and deformed
- Widespread anisotropy is observed at the base of Nazca slab where it penetrates the higher-viscosity lower mantle

Supporting Information:
- Supporting Information S1
- Table S1
- Table S2

Correspondence to:
S. Agrawal,
shubham.agrawal@anu.edu.au

Citation:
Agrawal, S., Eakin, C. M., Portner, D. E., Rodriguez, E. E., & Beck, S. L. (2020). The deformational journey of the Nazca slab from seismic anisotropy. *Geophysical Research Letters*, *47*, e2020GL087398. https://doi.org/10.1029/2020GL087398

Received 6 FEB 2020
Accepted 1 MAY 2020
Accepted article online 7 MAY 2020

This article was prematurely published without the authors' corrections. Corrections were made on 2 JUL 2020, to incorporate the authors' changes.

Abstract The Andean subduction zone is an excellent place to study deformation within a subducting slab as a function of depth, owing to the varying and well-resolved geometry of the subducting Nazca slab beneath South America. Here we combine the results of source-side shear wave splitting with the latest regional tomography model to isolate intraslab raypaths and determine the spatial distribution of anisotropy within the Nazca slab. We observe that in the upper mantle, the intraslab anisotropy appears strongest where the slab is most contorted, suggesting a strong link between anisotropy and subduction-related slab deformation. We identify a second source of anisotropy ($\delta t \sim 1$ s) within the subducting slab at lower mantle depths (660–800 km). The surrounding mantle and transition zone appear largely isotropic, with deep anisotropy concentrated within the slab as it deforms while entering the higher-viscosity lower mantle.

Plain Language Summary Few observations exist of how a tectonic plate deforms as it descends deep into the Earth's interior at a subduction zone. Carefully selected seismic waves that mostly travel through this subducting plate, or slab, provide some of the most direct measurements of how the slab behaves as it sinks through the upper mantle (0–410 km) and the mantle transition zone (410–660 km). Studying the polarization of seismic waves allows us to detect and infer the pattern of deformation within the Earth's interior. Using this technique, we find that the Nazca slab in the Andean subduction zone in South America has undergone internal deformation during the process of subduction, in particular where the slab's 3-D shape changes. Furthermore, we find that the deeper Nazca slab (≥660 km) appears to undergo further deformation as it interacts with the stiffer uppermost lower mantle.

1. Introduction

Studying how slabs deform as they subduct is critical for our understanding of subduction dynamics, earthquake behavior, and the forces which ultimately drive mantle convection and plate tectonics. Inferences of intraslab deformation, particularly nonelastic or viscous deformation, typically rely on indirect measurements or geodynamic modeling (e.g., Alpert et al., 2010; Wenk et al., 2006). Some of the most direct constraints on mantle deformation and dynamics come from the analysis of seismic anisotropy, defined simply as the directional dependence of seismic wave speed (e.g., Savage, 1999). The shear wave splitting technique, whereby a shear wave entering an anisotropic medium is split into two orthogonal quasi *S* waves, provides the most unambiguous detection of seismic anisotropy (e.g., Savage, 1999; Silver, 1996). By measuring the polarization of the faster quasi *S* wave, ϕ, and the time delay between the split waves, δt, the strength and geometry of the anisotropic structure can be inferred.

In the upper mantle, the presence of anisotropy is typically ascribed to either (i) solid-state deformation caused by mantle flow, aligning constituent anisotropic minerals through lattice preferred orientation (LPO) (e.g., Ismail & Mainprice, 1998), or (ii) shape preferred orientation of materials with distinct elastic properties, such as partial melts (e.g., Holtzman & Kendall, 2010). The dominant upper mantle mineral, olivine, is intrinsically anisotropic with a large single-crystal anisotropy (~18%) for shear waves (e.g., Ismail & Mainprice, 1998; Zhang & Karato, 1995) and is thus thought to be the main source of anisotropy in the upper mantle. Under typical upper mantle conditions, A-, C-, or E-type olivine LPO fabrics are thought to dominate, for which shear wave splitting of teleseismic shear waves results in fast polarization directions parallel to the horizontal shear direction (Karato et al., 2008).

In subduction zones, previous studies have suggested the presence of anisotropy in the mantle transition zone (MTZ) and uppermost-lower mantle (ULM) around subducting slabs (Ferreira et al., 2019; Lynner & Long, 2015; Nowacki et al., 2015; Walpole et al., 2017; Wookey et al., 2002). Most of these studies attribute the observed anisotropy to shearing of the surrounding mantle, which is predominantly composed of bridgmanite (perovskite-structured $(Mg,Fe)SiO_3$) (e.g., Hirose, 2002) and has recently been shown to be capable of deformation-induced LPO development (Miyagi & Wenk, 2016; Tsujino et al., 2016).

Direct measurements of intraslab anisotropy, particularly from shear wave splitting analysis, have been limited (Chen et al., 2015; Eakin et al., 2016; Huang et al., 2011). This is because the most commonly utilized phase for this procedure—SKS phases with near-vertical incidence (≤10°)—typically do not significantly sample the subducting slab. To capture long intraslab paths, certain optimal ray geometries are required, for example, a steeply dipping slab and/or seismic stations close to the trench. A new potentially fruitful avenue for exploration is the source-side splitting method (e.g., Long & Silver, 2009; Russo & Silver, 1994) in which anisotropy on the receiver side is corrected, allowing for the determination of anisotropy beneath the earthquake source. If the source-side method is applied to earthquakes that originate in the subducting plate with downdip raypaths traveling through the slab, then intraslab anisotropy and deformation can be investigated.

A favorable location for studying this relationship between slab geometry, anisotropy, and deformation is the Andean subduction zone (ASZ), where the Nazca slab displays dramatic along-strike variations in slab dip as it subducts beneath South America. Most notably, it forms two regions of large-scale flat slab subduction, one beneath Peru, and the second, beneath central Chile and Argentina (Ramos & Folguera, 2009). The extent of the Nazca slab, both along strike and in depth, has been illuminated recently by the SAM5_P_2019 *P* wave tomography model (Portner et al., 2020), providing a detailed picture of the contorted slab morphology at depth (Figures 1 and 3). Moreover, the ASZ has ample seismicity, including some of the world's deepest earthquakes (≥600 km), allowing for depth-dependent investigations of slab anisotropy.

Source-side splitting studies in the ASZ have focused either on the subslab mantle (Eakin & Long, 2013; Nowacki et al., 2015; Russo & Silver, 1994; Russo et al., 2010; Walpole et al., 2017) or the MTZ (Lynner & Long, 2015; Nowacki et al., 2015). One previous study has targeted slab anisotropy, but this was only for the Peruvian flat slab region (Eakin et al., 2016). This work is the first attempt to investigate intraslab anisotropy along the length of the ASZ, utilizing the most up-to-date regional *P* wave tomography model of the whole ASZ (Portner et al., 2020).

2. Events, Stations, and Methods

All earthquakes since 1985, spanning the ASZ from 0° to 40°S, with moment magnitude ≥5.5 and a source depth ≥100 km were selected. The hypocenter depth constraint ensures we select earthquakes from the subducting Nazca slab and not the overriding plate. In total, 351 earthquakes (Figure 1a and Figure S1 in the supporting information) were used out of which ~81% (286 events) were in the upper mantle and the remainder in the MTZ, with the deepest event at 631.3 km depth.

For the source-side splitting technique, the goal is to isolate the anisotropy beneath the earthquake source using direct *S* teleseismic phases. On average the lower mantle is isotropic (e.g., Panning & Romanowicz, 2006), therefore, the biggest potential source of error is the contribution from the receiver side anisotropy (from the upper mantle beneath the seismic station). We therefore only utilize stations rigorously tested and compiled by Eakin et al. (2018) that display apparent isotropy (i.e., null SKS splitting results) for a wide range of back azimuths (hereon referred to as "null" stations). Anisotropy beneath the receiver can therefore be safely neglected for similar teleseismic shear waves (epicentral distance: 40–80°) with steep incident angles beneath the station. A maximum epicentral distance of 80° is chosen to avoid contamination from D′′ anisotropy (e.g., Niu & Perez, 2004). Overall, 27 null stations fulfilled these criteria, plotted as stars in Figures 1a and S1 (station details in Table S1).

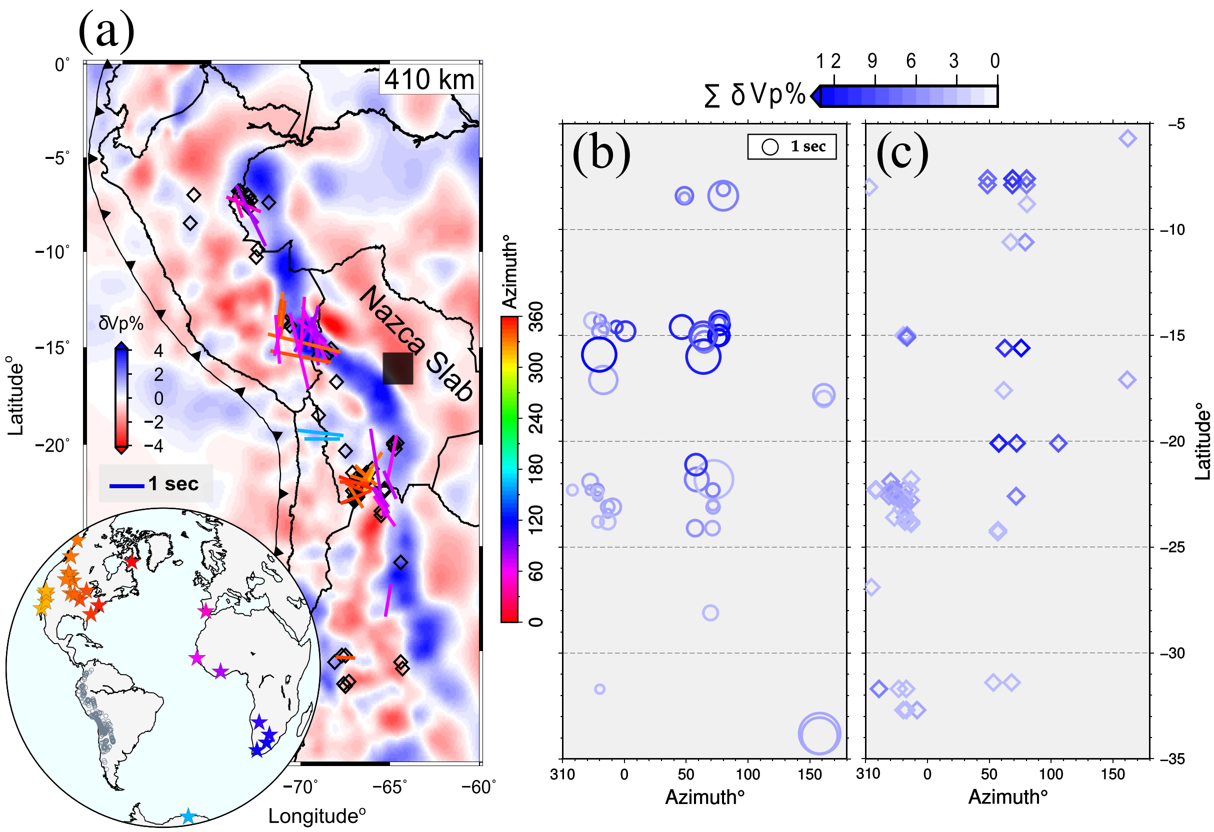

Figure 1. (a) Intraslab split (bars) and null (black diamonds) measurements ($\sum \delta Vp \geq 3$) for earthquakes ≤410 km depth plotted at ray pierce points on top of the 410 km *P* wave tomography depth section (Portner et al., 2020). The orientation of individual splits indicates the fast direction (ϕ) projected on the downgoing ray. The length of the bar is proportional to the delay time, δt and is colored by the azimuth according to the legend. In all cases, "azimuth" refers to the azimuth of the ray heading away from the source. The inset shows the distribution of earthquakes in South America and 27 null seismic stations (stars colored by azimuth). Intraslab split (b) and null (c) measurements plotted by latitude and azimuth. Size of circles is scaled by δt value and colored by the $\sum \delta Vp$ value.

To accurately extract splitting parameters (ϕ and δt) from the seismograms, we used the SplitLab software package (Wüstefeld et al., 2008). We applied a band-pass filter of 0.04 to 0.125 Hz and analyzed events for splitting using the rotation-correlation method (Bowman & Ando, 1987; Fukao, 1984) and the eigenvalue method (Silver & Chan, 1991). Split results were required to agree within 22.5° for ϕ and 0.5 s for δt between both methods (Figure S2). The fast direction measured at the receiver was then reflected across the azimuth to calculate the orientation beneath the source, that is, correcting for the downgoing ray versus upgoing ray. Null results required a visible shear wave pulse, above the noise, and with linear particle motion (i.e., evidence of no shear wave splitting). For a full description of the methodology, we direct the reader to our previous work (Eakin & Long, 2013; Eakin et al., 2018) and Text S2.

Our primary objective is to inspect the anisotropic properties of the Nazca slab. We therefore focus our attention on raypaths that appear confined to the slab throughout the upper mantle and MTZ using SAM5_P_2019. For each direct *S* ray, we calculate pierce points using TauP and the IASP91 velocity model (Crotwell et al., 1999; Kennett & Engdahl, 1991) at various depths (see Figure S3). We then determine the δVp value at each pierce point as given by SAM5_P_2019 (Figure S3) and sum together over all depths to obtain a parameter referred to as $\sum \delta Vp$ for each ray. The longer the ray spends inside the fast subducting slab, the higher the $\sum \delta Vp$ value will be, thus, serving as a proxy for residence time in the slab. We address the caveats of $\sum \delta Vp$ estimation in detail in supporting information Text S3.

Comparison with 3-D ray tracing demonstrates that rays are even more likely to be drawn into the slab than 1-D predictions using IASP91 (Figure S4 and Text S3), similar to experiments by Portner et al. (2020) (cf. Figure S4). Additionally, to demonstrate the sensitivity of *S* waves to the slab, we calculated the shear waves Fresnel zones (Text S4) and found them to be equivalent or smaller than the width of the slab at

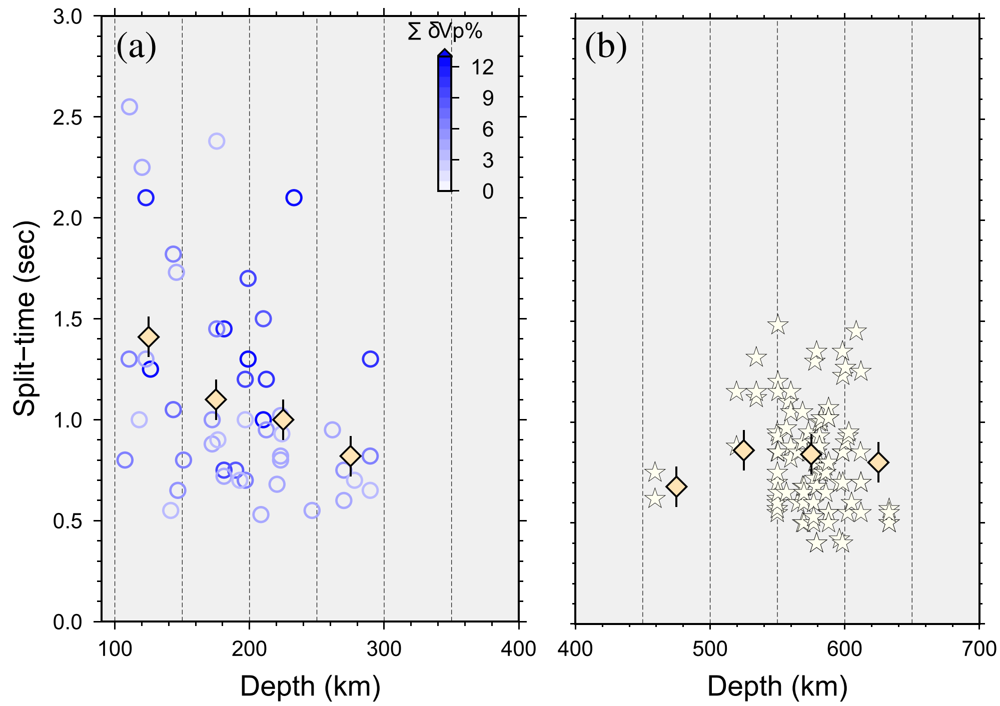

Figure 2. (a) Intraslab upper mantle split measurements plotted by earthquake depth and delay time. Each measurement is colored by the $\sum \delta Vp$ value. Orange diamonds are mean δt for each 50 km depth bin (dashed lines). (b) All deep split measurements plotted by earthquake depth and delay time.

each depth (Figure S7). This further confirms that our chosen raypaths are primarily sensitive to anisotropy within the slab rather than the surrounding mantle.

3. Upper Mantle Anisotropy in the Nazca Slab

Overall our source-side splitting analysis returned 492 individual split and 603 null measurements for all 27 seismic stations. These measurements were subdivided into 398 shallow events (upper mantle 100–410 km) and 94 deep events (MTZ 410–650 km) according to earthquake source depth.

For shallow events, a clear difference in splitting is seen between rays that primarily sample the subslab mantle and those that fall within or close to the slab (Figure S6), suggesting a source of intraslab anisotropy distinct to the surrounding mantle. Focusing on those rays with $\sum \delta Vp$ values $\geq$3, indicating paths through high-velocity material in the upper mantle, retrieves 48 split and 68 null measurements (Figure 1). In general, null results (black diamonds, Figure 1a) appear evenly distributed along the length of the Nazca slab (Figure 1c), whereas split measurements (colored bars, Figure 1a) seem concentrated in a handful of discrete locations (Figure 1b). Interestingly, the highest concentration of splitting measurements (19 splits) is found ~15°S where the strike of the Nazca slab bends considerably (~90°) between 200 and 400 km depths. This location also coincides with some of the largest delay times (2.1 s) and highest $\sum \delta Vp$ values found, indicated by larger and darker blue circles in Figure 1b.

Furthermore, intraslab split measurements from shallow events show depth dependent delay times (Figure 2a), suggestive of an upper mantle anisotropic source within the slab. The number of measurements with depth reflects the event distribution (Table S2) but interestingly both the mean (diamonds) and maximum δt values decrease monotonically with increasing depth, from a mean of 1.4 s at 125 km to 0.8 s at 275 km. The maximum delay time of 2.55 s was recorded on one of the shallowest events (117.3 km). For upper mantle events deeper than 250 km, the delay times are generally $\leq$1 s.

3.1. Has the Nazca Slab Fabric Been Overprinted?

The parameter $\sum \delta Vp$ is a compelling parameter to assess the ray-slab interaction. The most striking features that emerge are (i) there appears to be significant anisotropy inside the slab in the upper mantle (up to 2.1 s; Figure 2), and (ii) it is strongest around 15°S where the slab is most contorted. The presence of intraslab anisotropy between 10° and 17°S was previously investigated by Eakin et al. (2016) using two deep local events. They constrained intraslab anisotropy between 200 and 400km depths with fast directions that appeared to follow the strike of the slab as it bends at 15°S. These observations match well with our results in the same area, but now with more measurements we find greater variability in fast directions potentially due to a wider distribution of stations and associated azimuthal dependence.

Typically, anisotropy within a subducting slab is attributed to fossil anisotropy frozen-in from the time of oceanic lithosphere formation (e.g., Forsyth, 1975; Hess, 1964) predicting fast directions aligned with the direction of paleoplate spreading. Studies of anisotropy using surface waves show plate motion parallel fast directions within the Nazca plate before it subducts (e.g., Debayle & Ricard, 2013). Therefore, within the subducting Nazca slab, one would expect the anisotropic fast axis to be in an approximately downdip direction (Figure S8). For a shear wave traveling down through the slab, approximately parallel to the fast axis, only weak anisotropy (2%) and relatively small delay times (maximum 1.5 s) would be predicted (Figure S9). This is in contrast to certain locations, such as the bend at 15°S, where we observe strong splitting >2 s (Figures 1a and 1b). Instead, the full range of delay times (up to 2.6 s) can be explained if a new anisotropic fabric develops where the slab is undergoing significant deformation and strain rates are elevated, similar to previous suggestions by Reynard et al. (2010) and Eakin et al. (2016). While the strength of slabs is a subject of debate (Becker & Faccenna, 2009; King, 2001), evidence from seismic studies (e.g., Alpert et al., 2010) and modeling of the geoid (e.g., Zhong & Davies, 1999) indicate that subducting slabs must be weaker than expected despite their temperature, allowing for significant internal deformation and contorted slab morphologies. Furthermore, recent subduction models with deformation mechanism mapping indicate that dislocation creep, and therefore, LPO development is possible within slabs (Bessat et al., 2020). Estimates from the curvature of the Nazca slab contours suggest a bending strain of up to 1.4 (Eakin et al., 2016), which would be enough to begin to alter a previous frozen-in LPO (Boneh et al., 2015), but unlikely enough to fully align with the new shear direction. This could potentially add to the variability in fast directions we observe if a new steady state LPO has not yet been reached.

While the strains required to overprint LPO fabric within a slab may be controversial at present, it is clear, however, that the bulk of the intraslab anisotropy we observe is not the result of fossil fabric (Figures S8 and S9). Either this fabric is overprinted as we suggest or the anisotropy is the result of an alternate mechanism. For example, hydration and serpentinization of bending faults in the outer rise could also generate intraslab anisotropy (e.g., Faccenda et al., 2008). However, this is only expected to occur within the upper 10–20 km of the slab mantle (e.g., Shillington et al., 2015), which is not explicitly sampled by our intraslab rays (Figures 3 and 4). Moreover, it is difficult to explain why only a few select locations along the ASZ display intraslab splitting, unless serpentinization is also tied to slab deformation, where water has entered and weakened the slab.

4. Deep (≥500 km) Intraslab Anisotropy

The 70 deep events (source depths ≥410 km) returned 94 split and 185 null measurements (Figures 2b and 3), a lower occurrence of splits (34%) compared to events ≤410 km (49%; Table S2). The mean δt retrieved was 0.83 s, similar to the mean δt for the deepest upper mantle events (0.8 s at ∼275 km). Unlike the upper mantle, the deep results show little to no depth dependency, with consistent mean and maximum δt values across 500–650 km depth. These observations suggest the presence of an additional deep anisotropic zone in agreement with previous studies from the region (Lynner & Long, 2015; Nowacki et al., 2015). The fast directions, however, are complex, showing no predominant orientation (Figure 3).

From the 715 km depth section (Figure 3), it can be seen that most nulls move west out of the slab (black diamonds), while more splits tend to move east staying within the fast velocity slab (blue and purple bars). For stations in Africa, with rays moving eastward staying within the dipping slab, the percentage of splits is considerably higher at 50%, compared to only 29% for stations in North America and Antarctica (NW and south azimuths) (Table S3 and Figure 4).

4.1. Potential Source of Deep Anisotropy

The analyses revealed three important properties of deep anisotropy in the ASZ. First, there is no observable depth dependence, with similar delay times for events ranging from 550 to 640 km depth (Figure 2b). This points toward a common ULM source of anisotropy beneath 640 km, ruling out the MTZ as a major

10.1029/2020GL087398

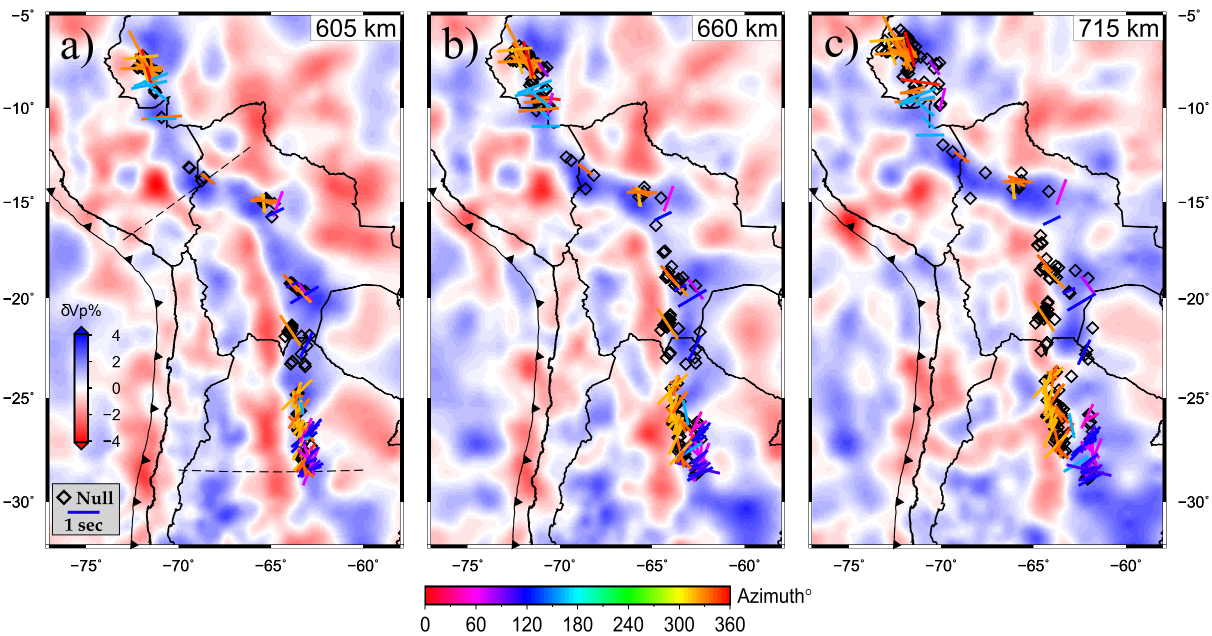

Figure 3. Split and null measurements (for earthquakes ≥410 km depth) plotted at ray pierce points on top of tomographic depth slices at 605, 660, and 715 km. Nulls are plotted as black diamonds of uniform size. For explanation of symbols, please refer to Figure 1a. (a)-(a′) and (b)-(b′) refer to cross sections shown in Figure 4.

contributor. Second, there is a higher chance of a shear wave undergoing splitting if the ray stays inside the slab (Figures 3 and 4), providing strong evidence for the presence of intraslab anisotropy in the ULM and not in the surrounding mantle. Previous studies were unable to make this distinction due to either a lack of downdip raypaths and/or an inability to assess slab traversing raypaths when only global tomographic (i.e., lower resolution) models are available (Foley & Long, 2011; Lynner & Long, 2015; Nowacki et al., 2015; Walpole et al., 2017; Wookey et al., 2002). Ferreira et al. (2019) recently inferred global radial anisotropy of the ULM beneath slabs but with a lateral model resolution of ~1,000 km and therefore unlikely to be able to pin-point anisotropy within a relatively narrow slab (Portner et al., 2020). Third, anisotropy is detected from deep seismicity throughout the ASZ (Figure 3) suggesting the presence of a widespread intraslab mechanism, rather than a few localized pockets of anisotropy.

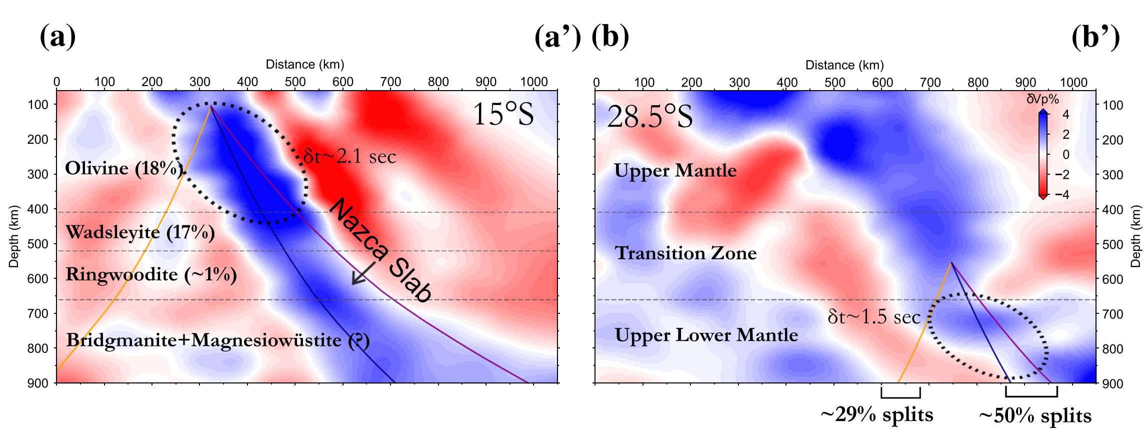

Figure 4. Vertical tomography slices displaying the subducting Nazca slab geometry for the profiles (a)-(a′) (left) and (b)-(b′) (right) as shown by dashed lines in Figure 3a. Three raypaths are shown for earthquakes at 100 km depth (left) and 550 km (right) traveling with azimuths 73° (purple), 120° (dark blue), and −42° (orange), which are representative for rays traveling to stations mostly in West Africa, South Africa, and North America, respectively. Dotted ellipses represent the inferred primary source of anisotropy, inside the slab in the upper mantle (left) and uppermost-lower mantle (right), with the maximum observed delay times. In the left figure, major minerals are shown with single crystal shear wave anisotropy values in brackets (Mainprice, 2010). In the right figure, the % splits are denoted for all westward (North America stations) and eastward (Africa) moving rays (see Table S3).

At 640 km depth, the major mineral present is ringwoodite, but it is very weakly anisotropic, ≤1% (Li et al., 2006; Mainprice, 2010) at MTZ pressures and thus is unlikely to contribute substantially to observed anisotropy. Alternatively, the presence of metastable olivine within the cold core of the subducting slab is a possibility (e.g., Green Ii & Burnley, 1989). However, this seems unrealistic given the diminishing presence of metastable olivine with depth and the 100 km path length required to explain ~1 s of δt even for events as deep as 620 km (Mainprice, 2010).

Another possibility within the slab is the presence of dense hydrous magnesium silicates (for reviews, see Mainprice & Ildefonse, 2009; Ohtani, 2005) or akimotoite from the transformation of low-alumina garnet (Shiraishi et al., 2008). Both of these minerals are highly anisotropic (up to 20%) and are stable at depths greater than 660 km but require relatively cool slab geotherms. The young (~41 Myr) and relatively warm Nazca slab is therefore not ideal for their formation. In addition, dense hydrous magnesium silicates require the olivine phase to be saturated (Green II et al., 2010), while estimates of global H_2O flux suggest that the relatively young Nazca slab is more than 90% dehydrated by 230 km depth (van Keken et al., 2011).

We therefore infer that the most probable remaining candidate is bridgmanite within the subducting slab, the major constituent mineral in the ULM. While some studies have suggested that it is possible for LPO to be inherited during phase transitions due to topotactical growth of new minerals (e.g., Mainprice et al., 1990), it seems improbable to maintain a coherent fabric after three successive phase transitions from olivine through to bridgmanite. Instead, recent mineral physics studies have found bridgmanite capable of developing LPO under shear strain and ULM conditions (Miyagi & Wenk, 2016; Tsujino et al., 2016), although the deformational framework and slip systems are currently less well understood. As the Nazca slab descends through the MTZ into the ULM, the increase in mantle viscosity would lead to greater resistance and the potential for widespread internal slab deformation (Ganguly et al., 2009). The presence of plentiful deep seismicity in the ASZ (Figure 3) with focal mechanism *P* axes suggesting downdip compression (e.g., Isacks & Molnar, 1971) is consistent with this view. Several previous studies have inferred bridgmanite LPO development in the mantle surrounding the slab due to high strain rates as the slab impinges on the lower mantle (Foley & Long, 2011; Lynner & Long, 2015; Walpole et al., 2017; Wookey et al., 2002). Our study, however, is the first to distinguish a primary source of deep anisotropy within the slab and therefore the first to propose widespread slab deformation capable of LPO development of bridgmanite. Alternatively, the anisotropic source would need to be much deeper (~900 km) directly beneath the slab tip (Figure 4). Our results therefore have implications for the inferred source and interpretation of deep anisotropy in other subduction zones studies, where the possibility of an intraslab source has been neglected.

5. Conclusion

We identify two distinct regions of anisotropy within the subducting Nazca slab, one in the upper mantle, and the other within the slab in the lower mantle (Figure 4). In the upper mantle, the strongest anisotropy appears most concentrated around a distinct latitude (~15°S) where the slab undergoes ~90° lateral bend in slab strike. This suggests development of new olivine LPO fabrics through significant subduction related deformation. Slab anisotropy can therefore provide important constraints on internal viscous deformation of slabs and their rheology, which are vital for modeling of subduction zone dynamics.

Significant anisotropy ($\delta t \sim 1$ s) in the ULM is detected that appears concentrated within the subducting slab (Figure 4). Given the depth and widespread lateral extent of deep anisotropy, its source is inferred to be LPO development of bridgmanite within the slab. As the slab impinges on the higher-viscosity lower mantle, it encounters increased resistance and therefore may deform internally. Studying deep anisotropy, combining splitting techniques with high-resolution images of slab geometry, therefore holds great potential to improve our understanding of the deformational evolution of slabs as they subduct through the mantle.

Acknowledgments
We thank three anonymous reviewers for their constructive comments. All seismic data used in this study were acquired from IRIS (https://www.iris.edu) Data Management Center. Full details of all 11 networks, including a list of DOIs, are provided in the supporting information (Text S1). We used the SplitLab 1.2.1 (Wüstefeld et al., 2008) updated by Rob Porritt (https://robporritt.wordpress.com/software/). S. A. and C. M. E. are currently supported by Australian Research Council Grant DE190100062. A table of all measurements made during this study can be found in the supporting information (Tables S5 and S6).

References

Alpert, L., Becker, T., & Bailey, I. (2010). Global slab deformation and centroid moment tensor constraints on viscosity. *Geochemistry, Geophysics, Geosystems*, *11*, Q12006. https://doi.org/10.1029/2010GC003301

Becker, T. W., & Faccenna, C. (2009). A review of the role of subduction dynamics for regional and global plate motions, *Subduction zone geodynamics* (pp. 3–34): Springer.

Bessat, A., Duretz, T., Hetényi, G., Pilet, S., & Schmalholz, S. M. (2020). Stress and deformation mechanisms at a subduction zone: Insights from 2-D thermomechanical numerical modelling. *Geophysical Journal International*, *221*(3), 1605–1625.

Boneh, Y., Morales, L. F., Kaminski, E., & Skemer, P. (2015). Modeling olivine CPO evolution with complex deformation histories: Implications for the interpretation of seismic anisotropy in the mantle. *Geochemistry, Geophysics, Geosystems*, *16*, 3436–3455. https://doi.org/10.1002/2015GC005964

Bowman, J. R., & Ando, M. (1987). Shear-wave splitting in the upper-mantle wedge above the tonga subduction zone. *Geophysical Journal International*, *88*(1), 25–41.

Chen, K. H., Tseng, Y.-L., Furumura, T., & Kennett, B. L. (2015). Anisotropy in the subducting slab: Observations from Philippine Sea plate events in Taiwan. *Geophysical Research Letters*, *42*, 10,248–10,255. https://doi.org/10.1002/2015GL066227

Crotwell, H. P., Owens, T. J., & Ritsema, J. (1999). The TauP toolkit: Flexible seismic travel-time and ray-path utilities. *Seismological Research Letters*, *70*(2), 154–160.

Debayle, E., & Ricard, Y. (2013). Seismic observations of large-scale deformation at the bottom of fast-moving plates. *Earth and Planetary Science Letters*, *376*, 165–177.

Eakin, C. M., & Long, M. D. (2013). Complex anisotropy beneath the Peruvian flat slab from frequency-dependent, multiple-phase shear wave splitting analysis. *Journal of Geophysical Research: Solid Earth*, *118*, 4794–4813. https://doi.org/10.1002/jgrb.50349

Eakin, C. M., Long, M. D., Scire, A., Beck, S. L., Wagner, L. S., Zandt, G., & Tavera, H. (2016). Internal deformation of the subducted Nazca slab inferred from seismic anisotropy. *Nature Geoscience*, *9*(1), 56.

Eakin, C. M., Rychert, C. A., & Harmon, N. (2018). The role of oceanic transform faults in seafloor spreading: A global perspective from seismic anisotropy. *Journal of Geophysical Research: Solid Earth*, *123*, 1736–1751. https://doi.org/10.1002/2017JB015176

Faccenda, M., Burlini, L., Gerya, T. V., & Mainprice, D. (2008). Fault-induced seismic anisotropy by hydration in subducting oceanic plates. *Nature*, *455*(7216), 1097.

Ferreira, A. M., Faccenda, M., Sturgeon, W., Chang, S.-J., & Schardong, L. (2019). Ubiquitous lower-mantle anisotropy beneath subduction zones. *Nature Geoscience*, *12*, 301–306.

Foley, B. J., & Long, M. D. (2011). Upper and mid-mantle anisotropy beneath the Tonga slab. *Geophysical Research Letters*, *38*, L02303. https://doi.org/10.1029/2010GL046021

Forsyth, D. W. (1975). The early structural evolution and anisotropy of the oceanic upper mantle. *Geophysical Journal International*, *43*(1), 103–162.

Fukao, Y. (1984). Evidence from core-reflected shear waves for anisotropy in the Earth's mantle. *Nature*, *309*(5970), 695.

Ganguly, J., Freed, A. M., & Saxena, S. K. (2009). Density profiles of oceanic slabs and surrounding mantle: Integrated thermodynamic and thermal modeling, and implications for the fate of slabs at the 660 km discontinuity. *Physics of the Earth and Planetary Interiors*, *172*(3-4), 257–267.

Green II, H. W., Chen, W.-P., & Brudzinski, M. R. (2010). Seismic evidence of negligible water carried below 400-km depth in subducting lithosphere. *Nature*, *467*(7317), 828.

Green Ii, H., & Burnley, P. (1989). A new self-organizing mechanism for deep-focus earthquakes. *Nature*, *341*(6244), 733.

Hess, H. (1964). Seismic anisotropy of the uppermost mantle under oceans. *Nature*, *203*(4945), 629.

Hirose, K. (2002). Phase transitions in pyrolitic mantle around 670–km depth: Implications for upwelling of plumes from the lower mantle. *Journal of Geophysical Research*, *107*(B4), 2078.

Holtzman, B. K., & Kendall, J.-M. (2010). Organized melt, seismic anisotropy, and plate boundary lubrication. *Geochemistry, Geophysics, Geosystems*, *11*, Q0AB06. https://doi.org/10.1029/2010GC003296

Huang, Z., Zhao, D., & Wang, L. (2011). Shear wave anisotropy in the crust, mantle wedge, and subducting pacific slab under northeast Japan. *Geochemistry, Geophysics, Geosystems*, *12*, Q01002. https://doi.org/10.1029/2010GC003343

Isacks, B., & Molnar, P. (1971). Distribution of stresses in the descending lithosphere from a global survey of focal-mechanism solutions of mantle earthquakes. *Reviews of Geophysics*, *9*(1), 103–174.

Ismail, W. B., & Mainprice, D. (1998). An olivine fabric database: An overview of upper mantle fabrics and seismic anisotropy. *Tectonophysics*, *296*(1-2), 145–157.

Karato, S.-I., Jung, H., Katayama, I., & Skemer, P. (2008). Geodynamic significance of seismic anisotropy of the upper mantle: New insights from laboratory studies. *Annual Review of Earth and Planetary Sciences*, *36*, 59–95.

Kennett, B., & Engdahl, E. (1991). Traveltimes for global earthquake location and phase identification. *Geophysical Journal International*, *105*(2), 429–465.

King, S. D. (2001). Subduction zones: Observations and geodynamic models. *Physics of the Earth and Planetary Interiors*, *127*(1-4), 9–24.

Li, L., Weidner, D. J., Brodholt, J., Alfe, D., & Price, G. D. (2006). Elasticity of Mg_2SiO_4 ringwoodite at mantle conditions. *Physics of the Earth and Planetary Interiors*, *157*(3-4), 181–187.

Long, M. D., & Silver, P. G. (2009). Shear wave splitting and mantle anisotropy: Measurements, interpretations, and new directions. *Surveys in Geophysics*, *30*(4-5), 407–461.

Lynner, C., & Long, M. D. (2015). Heterogeneous seismic anisotropy in the transition zone and uppermost lower mantle: Evidence from South America, Izu-Bonin and Japan. *Geophysical Journal International*, *201*(3), 1545–1552.

Mainprice, D. (2010). 2.16 seismic anisotropy of the deep earth from a mineral and rock physics perspective. *Treatise on Geophysics, Volume 2: Mineral Physics*, 437.

Mainprice, D., Humbert, M., & Wagner, F. (1990). Phase transformations and inherited lattice preferred orientation: Implications for seismic properties. *Tectonophysics*, *180*(2-4), 213–228.

Mainprice, D., & Ildefonse, B. (2009). Seismic anisotropy of subduction zone minerals–contribution of hydrous phases, *Subduction zone geodynamics* (pp. 63–84): Springer.

Miyagi, L., & Wenk, H.-R. (2016). Texture development and slip systems in bridgmanite and bridgmanite+ ferropericlase aggregates. *Physics and Chemistry of Minerals*, *43*(8), 597–613.

Niu, F., & Perez, A. M. (2004). Seismic anisotropy in the lower mantle: A comparison of waveform splitting of SKS and SKKS. *Geophysical Research Letters*, *31*, L24612. https://doi.org/10.1029/2004GL021196

Nowacki, A., Kendall, J-M., Wookey, J., & Pemberton, A. (2015). Mid-mantle anisotropy in subduction zones and deep water transport. *Geochemistry, Geophysics, Geosystems*, *16*, 764–784. https://doi.org/10.1002/2014GC005667

Ohtani, E. (2005). Water in the mantle. *Elements*, *1*(1), 25–30.

Panning, M., & Romanowicz, B. (2006). A three-dimensional radially anisotropic model of shear velocity in the whole mantle. *Geophysical Journal International*, *167*(1), 361–379.

Portner, D. E., Rodríguez, E. E., Beck, S., Zandt, G., Scire, A., Rocha, M. P., et al. (2020). Detailed structure of the subducted Nazca slab into the lower mantle derived from continent-scale teleseismic *P*-wave tomography. *Journal of Geophysical Research: Solid Earth*, *124*, e53955. https://doi.org/10.1029/2019JB017884

Ramos, V. A., & Folguera, A. (2009). Andean flat-slab subduction through time. *Geological Society, London, Special Publications*, *327*(1), 31–54.
Reynard, B., Nakajima, J., & Kawakatsu, H. (2010). Earthquakes and plastic deformation of anhydrous slab mantle in double Wadati-Benioff zones. *Geophysical Research Letters*, *37*, L24309. https://doi.org/10.1029/2010GL045494
Russo, R., Gallego, A., Comte, D., Mocanu, V., Murdie, R., & VanDecar, J. (2010). Source-side shear wave splitting and upper mantle flow in the Chile Ridge subduction region. *Geology*, *38*(8), 707–710.
Russo, R., & Silver, P. (1994). Trench-parallel flow beneath the Nazca plate from seismic anisotropy. *Science*, *263*(5150), 1105–1111.
Savage, M. (1999). Seismic anisotropy and mantle deformation: What have we learned from shear wave splitting? *Reviews of Geophysics*, *37*(1), 65–106.
Shillington, D. J., Bécel, A., Nedimović, M. R., Kuehn, H., Webb, S. C., Abers, G. A., et al. (2015). Link between plate fabric, hydration and subduction zone seismicity in Alaska. *Nature Geoscience*, *8*(12), 961.
Shiraishi, R., Ohtani, E., Kanagawa, K., Shimojuku, A., & Zhao, D. (2008). Crystallographic preferred orientation of akimotoite and seismic anisotropy of Tonga slab. *Nature*, *455*(7213), 657–660.
Silver, P. G. (1996). Seismic anisotropy beneath the continents: Probing the depths of geology. *Annual Review of Earth and Planetary Sciences*, *24*(1), 385–432.
Silver, P. G., & Chan, W. W. (1991). Shear wave splitting and subcontinental mantle deformation. *Journal of Geophysical Research*, *96*(B10), 16,429–16,454.
Tsujino, N., Nishihara, Y., Yamazaki, D., Seto, Y., Higo, Y., & Takahashi, E. (2016). Mantle dynamics inferred from the crystallographic preferred orientation of bridgmanite. *Nature*, *539*(7627), 81.
van Keken, P. E., Hacker, B. R., Syracuse, E. M., & Abers, G. A. (2011). Subduction factory: 4. Depth-dependent flux of H_2O from subducting slabs worldwide. *Journal of Geophysical Research*, *116*, B01401. https://doi.org/10.1029/2010JB007922
Walpole, J., Wookey, J., Kendall, J.-M., & Masters, T.-G. (2017). Seismic anisotropy and mantle flow below subducting slabs. *Earth and Planetary Science Letters*, *465*, 155–167.
Wenk, H.-R., Speziale, S., McNamara, A., & Garnero, E. (2006). Modeling lower mantle anisotropy development in a subducting slab. *Earth and Planetary Science Letters*, *245*(1-2), 302–314.
Wookey, J., Kendall, J-M., & Barruol, G. (2002). Mid-mantle deformation inferred from seismic anisotropy. *Nature*, *415*(6873), 777.
Wüstefeld, A., Bokelmann, G., Zaroli, C., & Barruol, G. (2008). SplitLab: A shear-wave splitting environment in Matlab. *Computers & Geosciences*, *34*(5), 515–528.
Zhang, S., & Karato, S.-I. (1995). Lattice preferred orientation of olivine aggregates deformed in simple shear. *Nature*, *375*(6534), 774.
Zhong, S., & Davies, G. F. (1999). Effects of plate and slab viscosities on the geoid. *Earth and Planetary Science Letters*, *170*(4), 487–496.

References From the Supporting Information

Gudmundsson, O. (1996). On the effect of diffraction on traveltime measurements. *Geophysical Journal International*, *124*(1), 304–314.
Karato, S.-I. (2008). Deformation of Earth materials. *An Introduction to the Rheology of Solid Earth*, *463*.
Long, M. D. (2010). Frequency-dependent shear wave splitting and heterogeneous anisotropic structure beneath the Gulf of California region. *Physics of the Earth and Planetary Interiors*, *182*(1-2), 59–72.
Lynner, C., & Long, M. D. (2013). Sub-slab seismic anisotropy and mantle flow beneath the Caribbean and Scotia subduction zones: Effects of slab morphology and kinematics. *Earth and Planetary Science Letters*, *361*, 367–378.
Lynner, C., & Long, M. D. (2014). Sub-slab anisotropy beneath the sumatra and circum-Pacific subduction zones from source-side shear wave splitting observations. *Geochemistry, Geophysics, Geosystems*, *15*, 2262–2281. https://doi.org/10.1002/2014GC005239
Rawlinson, N., & Sambridge, M. (2004). Wave front evolution in strongly heterogeneous layered media using the fast marching method. *Geophysical Journal International*, *156*(3), 631–647.
Walker, A. M., & Wookey, J. (2012). MSAT—A new toolkit for the analysis of elastic and seismic anisotropy. *Computers & Geosciences*, *49*, 81–90.
Walpole, J., Wookey, J., Masters, G., & Kendall, J. (2014). A uniformly processed data set of SKS shear wave splitting measurements: A global investigation of upper mantle anisotropy beneath seismic stations. *Geochemistry, Geophysics, Geosystems*, *15*, 1991–2010. https://doi.org/10.1002/2014GC005278